Available online at www.sciencedirect.com
ScienceDirect
Trans. Nonferrous Met. Soc. China 33(2023) 2328−2339
Transactions of Nonferrous Metals Society of China
www.tnmsc.cn

Microstructure, mechanical and wear properties of AZ31/CoCrFeNi composites fabricated by friction stir processing

Wen WANG*, Yuan FANG*, Pai PENG, Zhi-juan ZHANG, Peng HAN, Ting ZHANG, Zhi-hao LIU, Xiao-hu GUAN, Zhi WANG, Ke QIAO, Kuai-she WANG

National and Local Joint Engineering Research Center for Functional Materials Processing, Xi'an University of Architecture and Technology, Xi'an 710055, China

Received 2 March 2022; accepted 11 May 2022

Abstract: AZ31 magnesium (Mg) alloy composites reinforced with CoCrFeNi high-entropy alloy (HEA) particles were fabricated by friction stir processing (FSP). OM, SEM, EDS, and EBSD were used to characterize the microstructure of composites. Mechanical and wear properties of the composites were investigated by tensile, microhardness, and dry sliding wear tests. The results revealed that HEA particles were homogeneously distributed and exhibited good metallurgical bonding with Mg matrix. The yield strength, ultimate tensile strength, and microhardness of the composites were 80 MPa, 46 MPa, and HV 54.9 higher than those of the base metal (BM), respectively. Fine-grained strengthening was the main strengthening mechanism whose contribution rate on the yield strength was 43.9%. The average friction coefficient of the composites was decreased from 0.331 of BM to 0.240, and the wear mechanism was changed from adhesive wear of BM to abrasive wear.

Key words: friction stir processing; high-entropy alloy particles; magnesium matrix composite; interface layer; tensile properties; wear properties

1 Introduction

Magnesium (Mg) matrix composites have attracted significant attention due to their excellent specific strength, high hardness, and good wear properties. Mg matrix composites reinforced with ceramic particles are prone to crack and pore formation due to the mismatch of thermal expansion between the ceramic particles and Mg matrix, leading to unfavorable mechanical properties [1,2]. Therefore, it is imperative to seek a new reinforcement to render the excellent comprehensive performances to particle-reinforced Mg matrix composites.

High-entropy alloys (HEAs), as a new type of metallic materials, are composed of five or more principal elements with each elemental molar fraction in the range of 5−35 at.% [3]. Typically, HEAs exist as a stable solid solution with high strength, hardness [4], wear resistance [5] as well as excellent thermal stability [6]. Compared with that of ceramics, the thermal expansion coefficient of HEAs is similar to that of metals, thus, they exhibit a better interfacial wettability with the metallic matrix. Hence, HEAs can be used as an ideal reinforcement for Mg matrix composites.

For example, TUN et al [7,8] fabricated Mg matrix composites reinforced with AlMgLiCuZn particles by powder metallurgy. The dispersed HEA particles exhibited good interfacial bonding with Mg matrix, but clustered particles exhibited weak

* Wen WANG and Yuan FANG contributed equally to this work

Corresponding author: Wen WANG, Tel: +86-13720527194, E-mail: wangwen2025@126.com;
Kuai-she WANG, Tel: +86-13186002826, E-mail: wangkuaishe888@126.com

DOI: 10.1016/S1003-6326(23)66262-4

interfacial bonding. MENG et al [9−11] prepared an AlCoCrCuFeNi HEA coating on the Mg matrix surface by laser melt injection. Although the microhardness of the coating significantly increased, the dry sliding wear performance at room temperature decreased due to the formation of brittle intermetallic compound ($CuMg_2$) between the HEA particles and matrix. In summary, it is imperative to avoid interfacial debonding and the formation of brittle intermetallic compound between reinforced particles and matrix in particle-reinforced Mg matrix composites.

Friction stir processing (FSP), as a new severe plastic deformation technique, was developed based on the principle of friction stir welding (FSW) [12]. So far, Al [13], Mg [14], Cu [15], Ti [16], and steel [17] matrix composites have been successfully produced using FSP. Compared with traditional technologies for preparing particle-reinforced composite, FSP exhibits the following advantages. First, FSP is a solid-state processing technique, which can prevent the formation of brittle phases at the interface due to low processing temperature. Second, FSP can improve the mechanical properties of the composites by refining, homogenizing and densifying the microstructure simultaneously. Third, FSP renders precise control of microstructure by optimizing stir tool and processing parameters [18].

LI et al [19] fabricated 5083Al/$Al_{0.8}$CoCrFeNi composites by FSP. A new HEA (Al_3CoCrFeNi) was formed rather than intermetallic compound at the interface between particles and Al matrix, which enhanced interface bonding. Compared with those of the 5083Al matrix, the yield strength (YS) and ultimate tensile strength (UTS) of composites increased by 60 MPa and 65 MPa, respectively, and the microhardness increased by 56.1%. GAO et al [20] used FSP to prepare 5083Al/AlCoCrFeNi composites. The addition of the HEA particles resulted in the increase of hardness as well as the decrease of friction coefficient from 0.584 to 0.423. Similarly, YANG et al [21−23] fabricated 5083Al/AlCoCrFeNi composite using underwater FSP. The YS and UTS of the composites were 25.1% and 31.9% higher than those of Al matrix, respectively, while the composites maintained acceptable elongation. Meanwhile, the microhardness was increased by 68.8%, and the wear rate was decreased by 48.6%. The excellent performances of the composite were related to good metallurgical bonding between the particles and matrix.

In summary, it is effective to employ FSP to prepare composites. However, the fabrication of Mg matrix composites reinforced with HEA particles by FSP has been rarely reported. In this work, HEA particle-reinforced Mg matrix composites were synthesized by FSP. In addition, the effect of the incorporated HEA particles on the microstructure and mechanical properties of the composites was evaluated, as well as the interface characteristic between HEA particles and Mg matrix. This work intends to provide a novel ideal for the preparation of HEA particle-reinforced Mg matrix composites.

2 Experimental

2.1 Materials

A hot-rolled AZ31 Mg alloy plate with dimensions of 160 mm × 80 mm × 4 mm was used as the base material (BM). HEA particles were prepared by gas atomization with a nominal composition of CoCrFeNi (wt.%). Tables 1 and 2 summarize the chemical compositions of BM and HEA particles, respectively. The particles exhibited a spherical morphology with an average size of 17.5 μm (Fig. 1). Following the Boltzmann's hypothesis on the relationship between entropy complexity [24], the configurational entropy change (ΔS_{conf}) of HEA particles was calculated by Eq. (1):

$$\Delta S_{conf}=R\ln n \quad (1)$$

where R is the gas molar constant; n is the number of elements. The calculated value of entropy was 11.56 J/K.

Table 1 Chemical composition of BM (wt.%)

Al	Zn	Si	Mn	Fe	Ti	Mg
3.05	0.92	0.27	0.28	0.03	0.06	Bal.

Table 2 Chemical composition of HEA particles (wt.%)

Co	Cr	Fe	Ni
24.88	25.34	25.21	24.57

2.2 FSP preparation of composites

Figure 2(a) shows the preparation procedure of the composites. Firstly, a row of holes were machined along the center of the plate along the length direction (d1.5 mm, depth: 2 mm, edge spacing: 2.1 mm, number of holes: 28). Secondly,

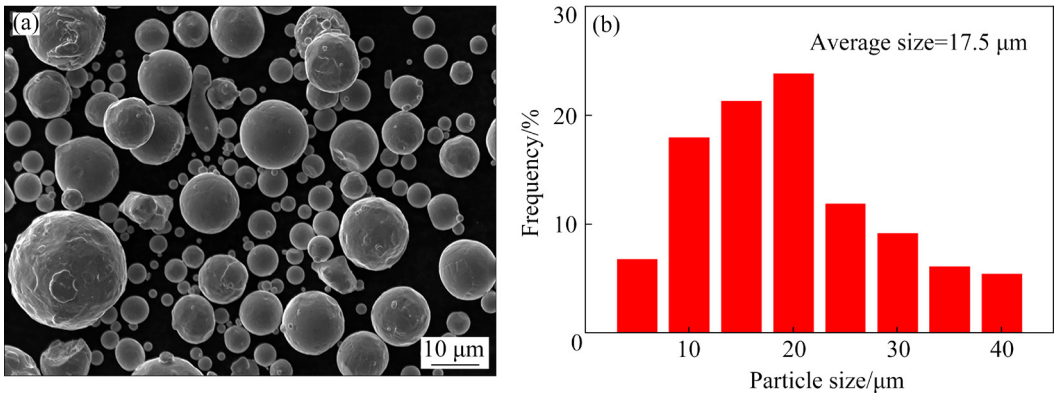

Fig. 1 Morphology (a) and size distribution (b) of HEA particles

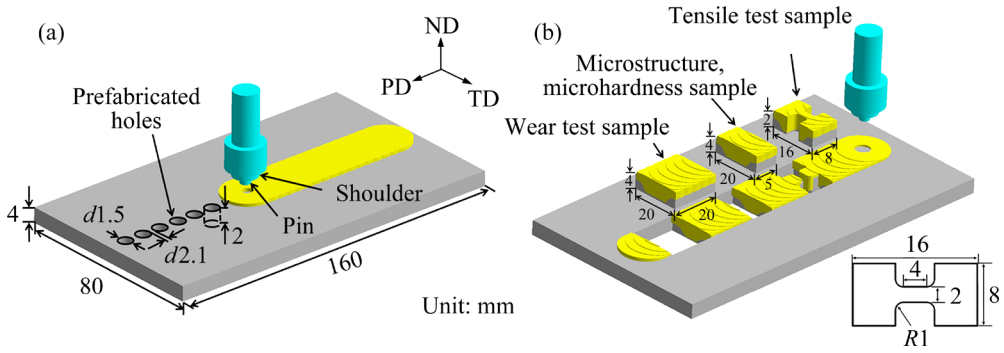

Fig. 2 Schematics of FSP (a), and test samples (b) (PD, TD and ND represent processing, transverse, and normal directions, respectively)

HEA particles were filled into the holes. Then, a pin-free stir tool with a diameter of 10 mm was used to prevent the particles from leaving the matrix during FSP. Finally, the plate was friction stir processed (FSPed) for four passes, and the processing direction of each pass was opposite to that of the previous one. The stir tool was made of H-13 steel consisting of a shoulder (d15 mm) and a simple threaded cylindrical pin (D: 5 mm, length: 2 mm). The rotation speed, processing speed, tilting angle, and processed distance were set at 1080 r/min, 30 mm/min, 2°, and 100 mm, respectively. Argon protection was utilized to prevent oxidation. For comparison, BM without HEA particles was subjected to FSP under the same parameters, which was denoted as the FSPed Mg sample. The sample with HEA particles was denoted as the FSPed + HEA Mg sample. The volume fraction (V_p) of the HEA particles in the processed zone was calculated by Eqs. (2)−(4):

$$V_p = \frac{V_{holes}}{V_{PZ}} \quad (2)$$

$$V_{holes} = nV_h \quad (3)$$

$$V_{PZ} = DLr \quad (4)$$

where V_{holes} is the volume of holes, V_{PZ} is the volume of processed zone (PZ), V_h is the volume of a hole, n is the number of holes, D is the pin diameter, L is the pin length, and r is the processed distance.

The calculated value of V_p was approximately 10%.

2.3 Characterization

The macrostructure and microstructure of BM, FSPed Mg, and FSPed + HEA Mg samples were characterized by optical microscopy (OM, Olympus GX51), scanning electron microscopy (SEM, JSM−6700F) equipped with energy-dispersive X-ray spectroscopy (EDS) and electron backscatter diffraction (EBSD). The metallographic specimens were mechanically polished and etched using a corrosive solution (4.2 g picric acid, 10 mL acetic acid, 10 mL water, and 100 mL absolute ethanol) for 10 s. The EBSD specimens were electrolytically polished in a perchlorate alcohol solution. The polishing voltage, temperature, and time were 12 V,

−20 °C, and 200 s, respectively.

Tensile samples with a gauge length of 4 mm, a width of 2 mm, and a thickness of 2 mm were machined perpendicularly to the processing direction (Fig. 2(b)). And then, tensile tests were performed on an Instron−8801 experimental machine at room temperature and an initial strain rate of 1×10^{-3} s^{-1}. The microhardness tests were conducted on the TD−ND plane using a 401MVD hardness tester with a load of 100 g and a dwell time of 10 s.

Wear tests were performed under dry sliding conditions using an MS-T3001 ball-on-disc wear tester with a GCr15 steel ball (ball diameter: 5 mm) at room temperature. The wear parameters included a normal load of 10 N, a rotation radius of 5 mm, a rotation speed of 200 r/min, and a total time of 900 s. Then, the wear morphology was characterized by laser confocal microscopy (Smart proof 5), and the wear tracks of the cross-section were depicted. The wear volume (V) and wear rate (K) were calculated according to Eqs. (5) and (6) [20], respectively.

$$V=Sl \tag{5}$$

$$K=\frac{V}{Fm} \tag{6}$$

where S and l are average values of the cross-sectional area and the length of the wear track, respectively, F is the normal load, and m is the sliding distance.

3 Results and discussion

3.1 Macrostructure

Figure 3 shows the cross-sections of FSPed and FSPed + HEA Mg samples. Obvious basin-shaped PZ can be observed in the FSPed and FSPed + HEA Mg samples. The width of PZ zone was equivalent to the diameter of the shoulder, and the depth of PZ was slightly longer than the length of the stir pin. Material flow tracks were clearly observed in the PZ, and there were no obvious defects, such as cavities and tunnels. The black boxes represent sampling locations for subsequent microstructure characterization.

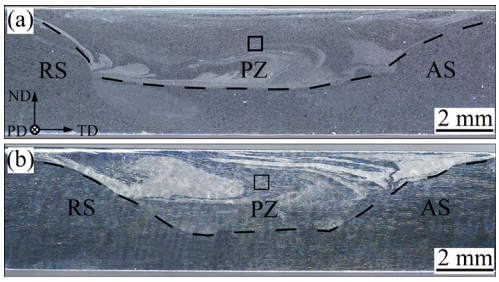

Fig. 3 Cross-sections of FSPed (a) and FSPed + HEA (b) Mg samples (AS and RS represent advancing sides and retreating sides, respectively)

3.2 Microstructure

Figures 4(a−c) show the inverse pole figures (IPF) of BM, FSPed Mg, and FSPed + HEA Mg samples, respectively. The BM sample exhibited heterogeneous and coarse grains. The average grain size (GS) was determined to be ~20 μm by the mean linear intercept technique (Fig. 4(a)). The FSPed Mg sample exhibited equiaxed grains with an average grain size of ~9 μm (Fig. 4(b)). This result indicated that PZ underwent severe plastic deformation and dynamic recrystallization, which can effectively refine grains during FSP. For FSPed + HEA Mg sample, the average grain size was reduced to ~4 μm (Fig. 4(c)). As shown in Fig. 4(d), high-density dislocations caused by the mismatch of the thermal expansion coefficient and elastic modulus between HEA particles and Mg matrix provided nucleation sites for recrystallized grains during FSP. This mechanism was particle induction nucleation (PSN) [21], leading to grain refinement.

Figure 5(a) shows the morphology and distribution of HEA particles in the FSPed + HEA Mg sample. The HEA particles were homogeneously distributed in the matrix without clear agglomeration. Multi-pass FSP in the reverse direction can effectively eliminate the uneven fluidity on the AS and RS due to the difference in temperature and strain. Most particles were mechanically crushed to approximately 1 μm, while some particles with a diameter of ~20 μm were still maintained. Figure 5(b) shows EDS mapping of elements in a single particle. Four elements in HEA particles were homogeneously distributed. The interface between the particle and matrix exhibited excellent integrity without defects, such as cracks or weak bonding.

Figure 6 shows the interfacial morphology and atomic diffusion between a single HEA particle and Mg matrix. A smooth and uniform interfacial layer was observed, with a mean thickness of ~500 nm (Fig. 6(a)), which was significantly less than that

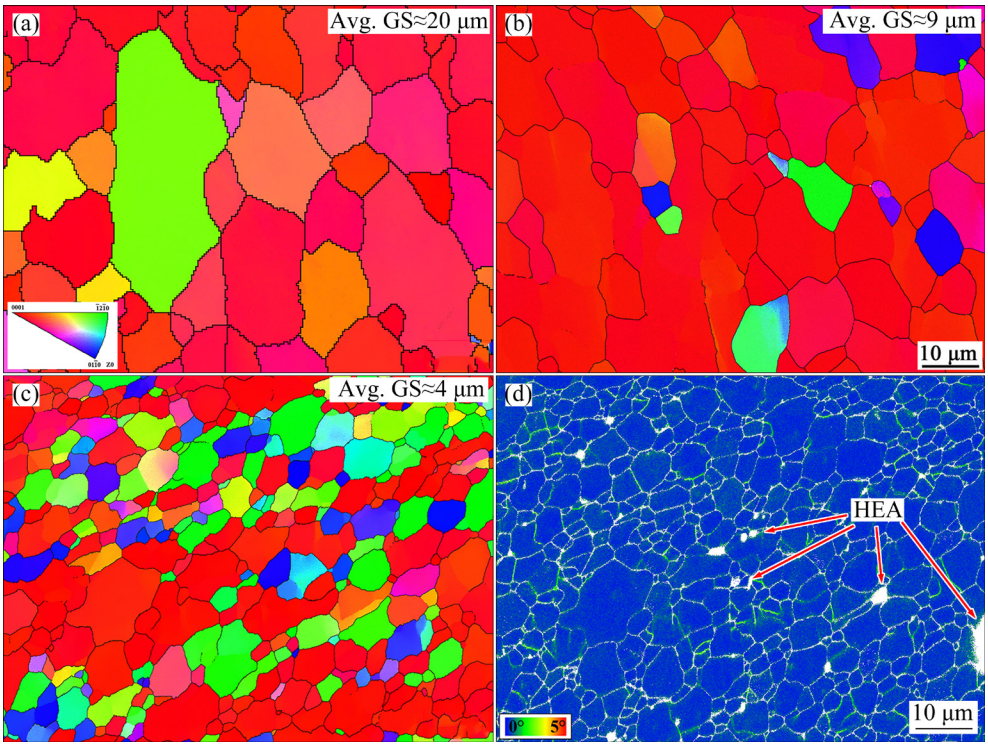

Fig. 4 Inverse pole figures of BM (a), FSPed Mg (b) and FSPed + HEA Mg (c) samples, and KAM map of FSPed + HEA Mg sample (d)

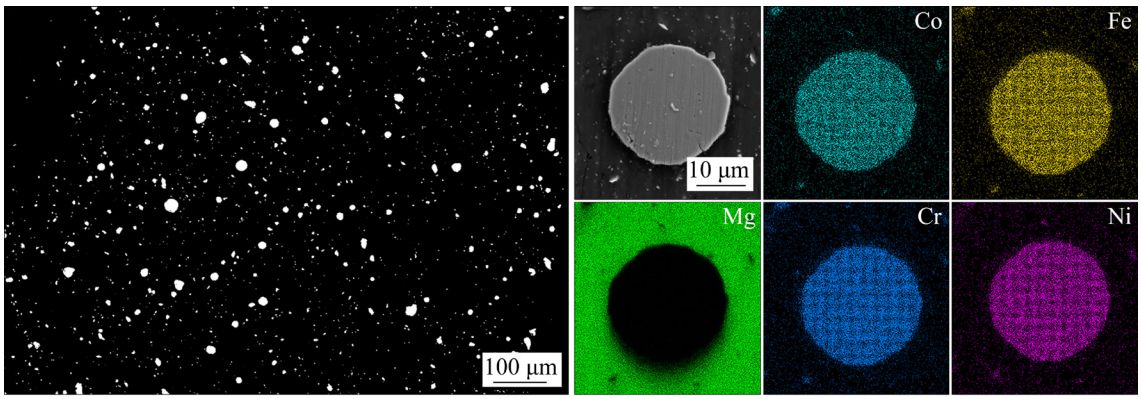

Fig. 5 Morphology and distribution of HEA particles in FSPed + HEA Mg sample (a), and EDS result of single particle (b)

produced by laser melt injection, laser additive synthesis, and spark plasma sintering [25−27]. Generally, a thin interfacial layer is beneficial to interfacial bonding and load transfer during plastic deformation in composites. Figure 6(b) shows the EDS line scanning result corresponding to the white arrow shown in Fig. 6(a). The interdiffusion occurred between the HEA particle and Mg matrix. Table 3 summarizes the elemental contents of the HEA particle near the interface (P_1), the interfacial layer (P_2), and matrix near the interface (P_3) in Fig. 6(a). The main elements were Co, Cr, Fe, Ni, and a few Mg at Point P_1, while Mg was the main element at Point P_3. The total content of Co, Cr, Fe, and Ni was equivalent to that of Mg at Point P_2. Moreover, the proportion of Co, Cr, Fe, and Ni at the three points was similar, indicative of no element segregation in HEA particles during FSP.

Figure 7 shows the grain boundary of BM, FSPed Mg, and FSPed + HEA Mg samples. Red and black lines represent low-angle grain boundaries (LAGBs, 2°−15°) and high-angle grain boundaries

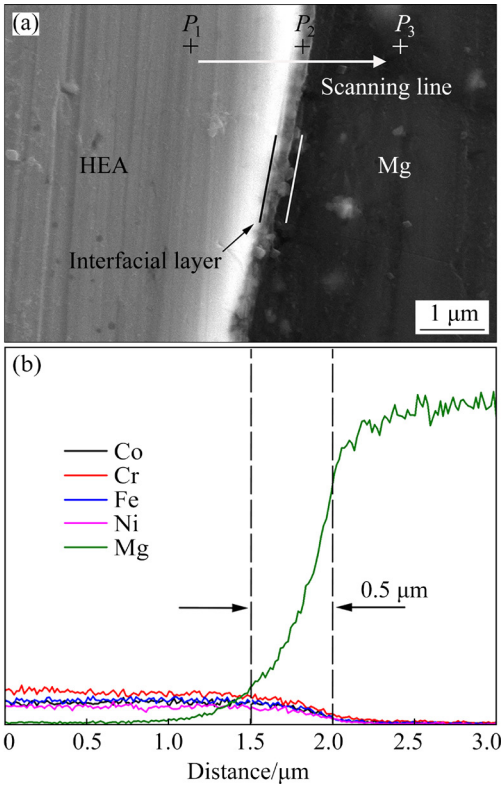

Fig. 6 Interfacial morphology of single HEA particle and Mg matrix (a), and corresponding EDS result (b)

Table 3 Chemical compositions of Points P_1, P_2 and P_3 (wt.%)

Point	Mg	Co	Cr	Fe	Ni
P_1	1.56	23.87	24.38	25.45	24.74
P_2	55.71	10.66	11.13	11.48	11.02
P_3	82.92	4.26	4.64	4.05	4.13

(HAGBs, >15°), respectively. The proportions of HAGBs in BM, FSPed Mg, and FSPed + HEA Mg samples were 94.5%, 58.3% and 73.3%, respectively. Notably, for the FSPed and FSPed + HEA Mg samples, LAGBs were entangled inside the grains to form fine recrystallized grains (as marked by the black arrow in Figs. 7(b, c)), indicative of the occurrence of continuous dynamic recrystallization (CDRX) during FSP [28]. Under the action of high strain and friction heat, a large number of dislocations were generated inside the grain and gradually accumulated to form dislocation walls, which further absorbed dislocation to form LAGBs. Then, the substructures and LAGBs transformed to HAGBs.

Figure 8 shows the pole figures of BM, FSPed Mg, and FSPed + HEA Mg samples. BM exhibits

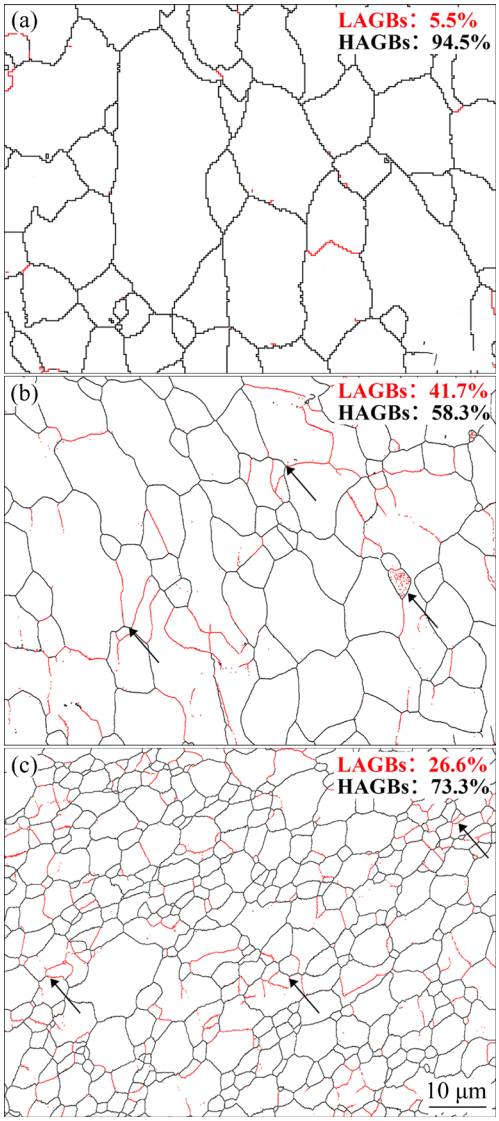

Fig. 7 Grain boundary maps of BM (a), FSPed Mg (b), and FSPed + HEA Mg (c) samples

a rolling texture with the maximum pole density of 26.7 (Fig. 8(a)). After FSP, the maximum pole density increases to 59.6 (Fig. 8(b)). The Mg alloy exhibits a close-packed hexagonal crystal structure, thus the basal slip can be easily activated due to lower critical shear stress than those of the cylindrical and pyramidal slips, leading to obvious change in the basal texture after FSP [29]. The maximum pole density of the FSPed + HEA Mg sample decreased to 19.4 (Fig. 8(c)), indicating the weakened texture due to the addition of HEA particles.

3.3 Tensile properties

Figure 9 shows the tensile properties of BM, FSPed Mg, and FSPed + HEA Mg samples at room

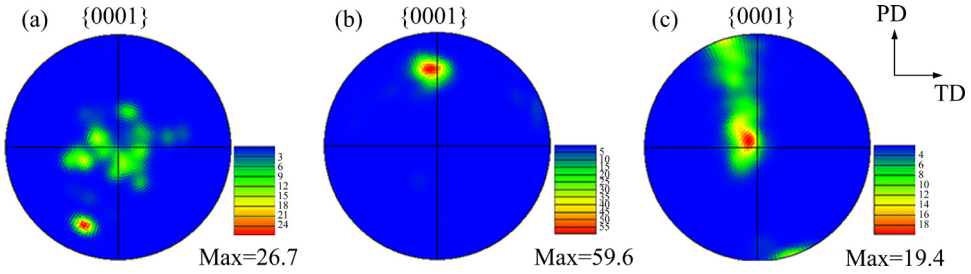

Fig. 8 Pole figures of BM (a), FSPed Mg (b), and FSPed + HEA Mg (c) samples

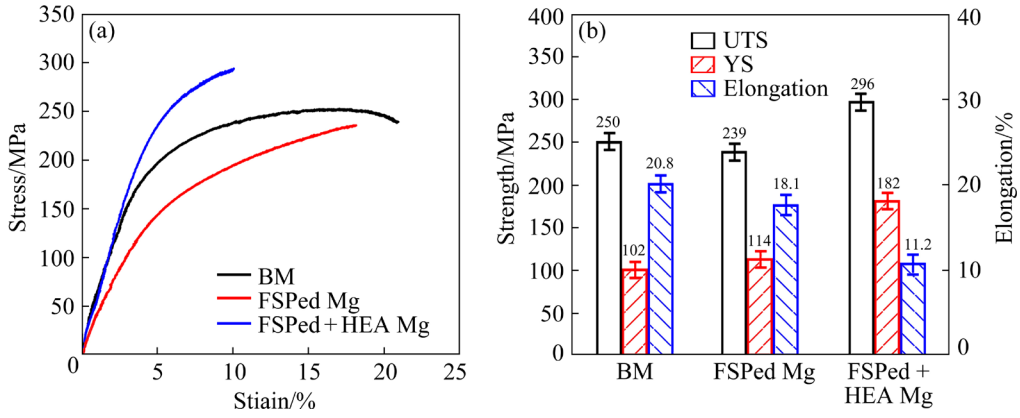

Fig. 9 Tensile properties of BM, FSPed Mg, and FSPed + HEA Mg samples

temperature. The YS, UTS, and elongation of the BM sample were 102 MPa, 250 MPa, and 20.8%, respectively. Compared with those of BM, the YS of the FSPed Mg sample was increased to 114 MPa, while the UTS and elongation of the FSPed Mg sample decreased to 239 MPa and 18.1%, respectively. The YS and UTS of the FSPed + HEA Mg sample were increased to 182 MPa and 296 MPa, respectively, while the elongation decreased to 11.2%.

With the addition of HEA particles, the YS of the composite was enhanced. The strengthening mechanisms of the composite included fine-grained strengthening, Orowan strengthening, thermal expansion mismatch strengthening, and load transfer effect [30].

Fine-grained strengthening ($\Delta\sigma_{\mathrm{H}}$) can be calculated by Eq. (7) [31]:

$$\Delta\sigma_{\mathrm{H}}=\sigma_0+\frac{k_{\mathrm{y}}}{\sqrt{d}} \tag{7}$$

where σ_0 is the friction stress (10 MPa for the AZ31 Mg alloy); k_{y} is the stress concentration factor (160 MPa·μm$^{1/2}$); d is the average grain size (4 μm).

Orowan strengthening ($\Delta\sigma_{\mathrm{Orowan}}$) can be calculated by Eq. (8) [32]:

$$\Delta\sigma_{\mathrm{Orowan}}=\frac{0.13Gb}{\lambda}\ln\frac{d_{\mathrm{p}}}{2b} \tag{8}$$

where G and b are the shear modulus (18 GPa) and amplitude of Burgers vector (0.325 nm) [33] of the AZ31 alloy, respectively; d_{p} is the average diameter of HEA particles (1 μm); λ is the average inter- particle spacing. The value of λ can be calculated by Eq. (9) [32]:

$$\lambda=d_{\mathrm{p}}\left[\left(\sqrt[3]{\frac{1}{2V_{\mathrm{p}}}}\right)-1\right] \tag{9}$$

where V_{p} is the volume fraction of the HEA particles (10%).

Thermal expansion mismatch strengthening ($\Delta\sigma_{\mathrm{CTE}}$) can be calculated by Eq. (10) [32]:

$$\Delta\sigma_{\mathrm{CTE}}=\alpha Gb\sqrt{\frac{12\Delta T\Delta CV_{\mathrm{p}}}{bd_{\mathrm{p}}\left(1-V_{\mathrm{p}}\right)}} \tag{10}$$

where α is a proportional constant (1.25); ΔT is the temperature change from processing temperature (500 °C) to room temperature (25 °C); ΔC is the difference in thermal expansion coefficient between the HEA particles and matrix (26.23×10^{-6} K^{-1}) [30].

Load transfer effect ($\Delta\sigma_{\mathrm{LT}}$) can be calculated by Eq. (11) [33]:

$$\Delta\sigma_{LT}=\frac{1}{2}V_p\sigma_{m0} \quad (11)$$

where σ_{m0} is the YS of BM (102 MPa).

SANATY-ZADEH [34] proposed that the strengthening effect of the above strengthening mechanisms was not equivalent. The theoretical YS value of the composites can be calculated by the Klein model, which can be calculated by Eq. (12):

$$\sigma_{YS}=\sigma_0+\sqrt{\Delta\sigma_H{}^2+\Delta\sigma_{Orowan}{}^2+\Delta\sigma_{CTE}{}^2+\Delta\sigma_{LT}{}^2} \quad (12)$$

The calculated values of $\Delta\sigma_H$, $\Delta\sigma_{Orowan}$, $\Delta\sigma_{CTE}$ and $\Delta\sigma_{LT}$ were 90, 46.1, 20.6, and 5.1 MPa, respectively, thus, the theoretical value of YS was 205 MPa. Fine-grained strengthening was the main factor, with a contribution rate of 43.9%, and the contribution rates of the other three mechanisms were 22.5%, 10%, and 2.4%, respectively. The experimentally obtained YS of the composites was 184 MPa, which was slightly less than the theoretically calculated value because the HEA particles were not completely broken during FSP, and some larger HEA particles were still retained.

Notably, although the HEA particles can significantly refine the grains of the Mg matrix by PSN, the strengthening generated by broken HEA particles was not clear due to their large size. Therefore, the Mg matrix composites reinforced by nano-sized HEA particles will be prepared in our future work, and the effect of particle size on the microstructure and mechanical properties will be clarified.

3.4 Microhardness

Figure 10 shows the microhardness profiles across the cross-section of the BM, FSPed Mg, and FSPed + HEA Mg samples. The average microhardness of the BM sample was HV 55.7, and the average microhardness of the PZ of FSPed Mg sample was increased to HV 81.4. The average microhardness of the PZ of FSPed + HEA Mg sample reached HV 110.6, which was 98.6% higher than that of the BM sample. The FSPed + HEA Mg sample exhibited the highest hardness, which was mainly attributed to the grain refinement. Moreover, the fine and uniform distribution of HEA particles in the matrix may enhance the microhardness of composites via Orowan strengthening [35]. In addition, thermal expansion coefficient mismatch strengthening as well as the load transfer effect could be considered as other reasons for enhanced microhardness [36].

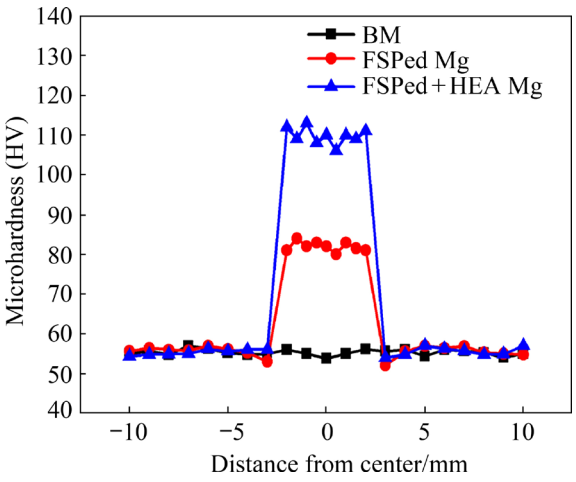

Fig. 10 Microhardness profiles across cross-section of BM, FSPed Mg and FSPed + HEA Mg samples

3.5 Wear behavior

Figure 11 shows the friction coefficients of the BM, FSPed Mg, and FSPed + HEA Mg samples. The average friction coefficient of the FSPed Mg sample was 0.313, which was 5.4% less than that of the BM sample (0.331) due to the increase in the microhardness of the composites as a result of grain refinement. The average friction coefficient of the FSPed + HEA Mg sample was reduced to 0.240, which was 23.3% and 27.5% less than those of the FSPed Mg and BM samples, respectively. The FSPed + HEA Mg sample exhibited the lowest average friction coefficient because the hardest surface involved the smallest contact area under a constant applied load [37].

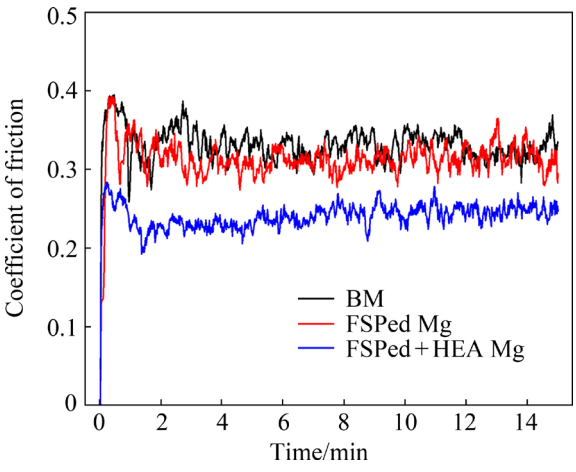

Fig. 11 Friction coefficients of BM, FSPed Mg, and FSPed + HEA Mg samples

Table 4 summarizes the results of the wear test of the BM, FSPed Mg, and FSPed + HEA Mg samples. BM exhibited the highest wear loss and wear rate. After FSP, the wear rate of the composites decreased due to the refinement of microstructure and the improvement of microhardness. According to the Archard formula (Eq. (9)), the wear rate was inversely proportional to the microhardness [38]:

$$Q=KFD/H \quad (13)$$

where Q is the wear volume per sliding distance; H is the microhardness of the wear surface. The wear rate of the FSPed + HEA Mg sample was 18.8% and 15.6% less than that of the BM and FSPed Mg samples, respectively, because the FSPed + HEA Mg sample exhibited the lowest friction coefficient and the highest surface hardness.

Figures 12(a, b) show the wear track of BM sample with a width of 1043 μm. Delamination and wear debris were clearly observed on the surface.

Table 4 Experiment results of sliding wear

Sample	Average area of wear track/μm^2	Wear volume/mm^3	Wear rate/(10^{-4}mm^3·N^{-1}·m^{-1})
BM	28475	0.8946	9.49
FSPed Mg	27427	0.8616	9.14
FSPed + HEA Mg	23118	0.7263	7.71

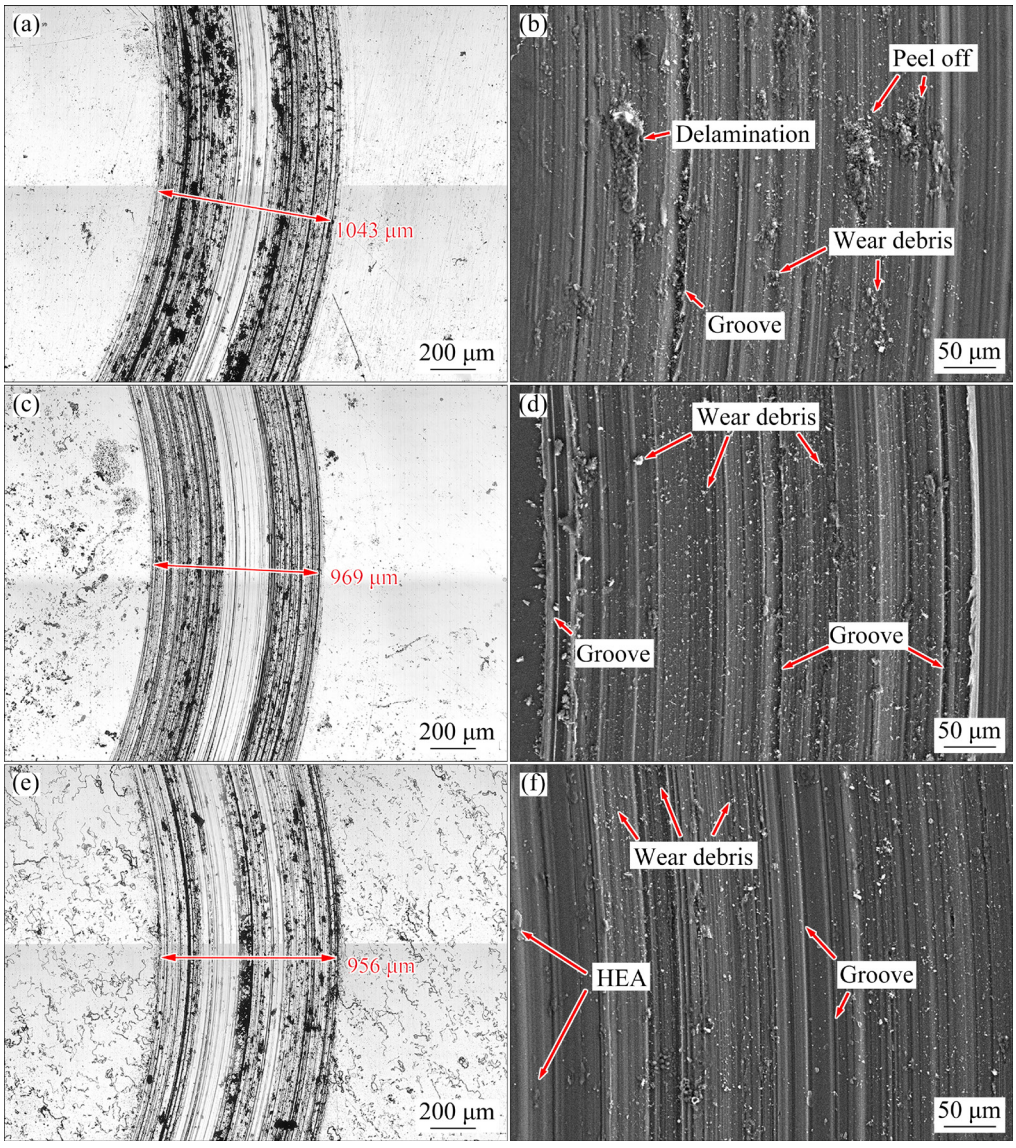

Fig. 12 Wear surfaces of BM (a, b), FSPed Mg (c, d), and FSPed + HEA Mg (e, f) samples

Under dry slip condition, the wear mechanism of the BM sample was adhesive wear. Micro-cracks nucleated on the subsurface of the sample and moved along the wear track. By the propagation of the micro-cracks to a certain extent, the matrix peeled off and formed delamination [39]. The peeled debris entered into the friction pair, affording three-body wear (sample/wear debris/friction pair), and subsequently resulting in the instantaneous increase of the friction coefficient (Fig. 11). Moreover, grooves were also clearly observed on the sample surface.

Figures 12(c, d) show the wear track of FSPed Mg sample with a width of 969 μm. Compared with the BM sample, the FSPed Mg sample displayed a small quantity of wear debris, with no obvious delamination mainly because of the improved deformability of the Mg matrix by FSP. As a result, the formation of micro-cracks in the subsurface is inhibited. This indicated that the wear mechanism of the FSPed Mg sample was changed to abrasive wear.

Figures 12(e, f) show the wear track of FSPed + HEA Mg sample with a width of 956 μm. The addition of HEA particles further increased the microhardness of the FSPed + HEA Mg sample, leading to shallower grooves and less wear debris than those observed in the FSPed Mg sample, indicating that wear was weakened and the wear mechanism changed to two-body wear (sample/ wear pair).

4 Conclusions

(1) During FSP, the HEA particles were homogeneously distributed in the Mg matrix and formed a good interfacial bonding with the matrix. Cracks or brittle intermetallic compound was not formed at the interface. The thickness of the diffusion layer was ~500 nm.

(2) FSP resulted in the average grain size, and the proportion of HAGBs and pole density of FSPed Mg sample changed from 20 μm, 94.5% and 26.7 to 9 μm, 58.3% and 59.6, respectively. The addition of HEA particles further refined the grains to 4 μm, and reduced the proportion of HAGBs and pole density to 73.4% and 19.4, respectively, due to the PSN mechanism.

(3) The YS, UTS and microhardness of the composite were 80 MPa, 46 MPa and HV 54.9 higher than those of BM, respectively. The strengthening mechanisms included fine-grained strengthening, Orowan strengthening, thermal expansion mismatch strengthening and load transfer effect, and their corresponding contribution rates on the YS were 43.9%, 22.5%, 10% and 2.4%, respectively.

(4) The average friction coefficient and wear rate of the HEA particle reinforced Mg matrix composite were 27.5% and 18.8% less than those of BM, respectively. The main wear mechanism was changed from adhesive wear (BM) to abrasive wear.

Acknowledgments

The authors gratefully acknowledge the sponsorship from the National Natural Science Foundation of China (Nos. U1760201, 52034005, 51974220), the Key Research and Development Program of Shaanxi Province, China (Nos. 2020ZDLGY13-06, 2017ZDXM-GY-037), the Innovation Capacity Support Project of Shaanxi Province-Nova Program, China (No. 2020KJXX-077), and the Science Fund for Distinguished Young Scholars in Universities of Shaanxi Province, China.

References

[1] LUO D, PEI C H, RONG J, WANG H Y, LI Q, JIANG Q C. Microstructure and mechanical properties of SiC particles reinforced Mg−8Al−1Sn magnesium matrix composites fabricated by powder metallurgy [J]. Powder Metallurgy, 2015, 58: 349−353.

[2] KHANDELWAL A, MANI K, SRIVASTAVA N, GUPTA R, CHAUDHARI G P. Mechanical behavior of AZ31/Al_2O_3 magnesium alloy nanocomposites prepared using ultrasound assisted stir casting [J]. Composites: Part B, 2017, 123: 64−73.

[3] YEH J W, CHEN S K, LIN S J, GAN J Y, CHIN T S, SHUN T T, TSAU C H, CHANG S Y. Nanostructured high-entropy alloys with multiple principal elements: Novel alloy design concepts and outcomes [J]. Advanced Engineering Materials, 2004, 6(5): 299−303.

[4] ZHANG Lin, SONG Ruo-kang, QU Guo-xin, LU Tong. Effect of nitrogen on microstructure and mechanical properties of $CrMnFeVTi_6$ high entropy alloy [J]. Transactions of Nonferrous Metals Society of China, 2021, 31: 2415−2427.

[5] CHEN Ming, LAN Li-wei, SHI Xiao-hui, YANG Hui-jun, ZHANG Ming, QIAO Jun-wei. The tribological properties of $Al_{0.6}$CoCrFeNi high-entropy alloy with the σ phase precipitation at elevated temperature [J]. Journal of Alloys and Compounds, 2019, 777: 180−189.

[6] CAO B X, YANG T, FAN L, LUAN J H, JIAO Z B, LIU C T.

Refractory alloying additions on the thermal stability and mechanical properties of high-entropy alloys [J]. Materials Science & Engineering A, 2020, 797: 140020.

[7] TUN K S, GUPTA M. Enhanced mechanical properties and near unity yield asymmetry in equiatomic high entropy alloy particles reinforced magnesium composites [J]. Journal of Alloys and Compounds, 2019, 810: 151909.

[8] TUN K S, ZHANG Yu-ming, PARANDE G, MANAKARI V, GUPTA M. Enhancing the hardness and compressive response of magnesium using complex composition alloy reinforcement [J]. Metals, 2018, 8: 276.

[9] MENG Guang-hui, YUE T M, LIN Xin, YANG Hai-ou, XIE Hui, DING Xu. Laser surface forming of AlCoCrCuFeNi particle reinforced AZ91D matrix composites [J]. Optics & Laser Technology, 2015, 70: 119−127.

[10] MENG Guang-hui, LIN Xin, XIE Hui, WANG Chen, WANG Shuan-qiang, DING Xu. Reinforcement and substrate interaction in laser surface forming of AlCoCrCuFeNi particle reinforced AZ91D matrix composites [J]. Journal of Alloys and Compounds, 2016, 672: 660−667.

[11] MENG G H, LIN X, XIE H, YUE T M, DING X, SUN L, QI M. The effect of Cu rejection in laser forming of AlCoCrCuFeNi/Mg composite coating [J]. Materials & Design, 2016, 108: 157−167.

[12] MISHRA R S, MA Z Y. Friction stir welding and processing [J]. Materials Science and Engineering R, 2005, 50: 1−78.

[13] VICTOR CHRISTY J, ISMAIL MOURAD A H, SHERIF M M, SHIVAMURTHY B. Review of recent trends in friction stir welding process of aluminum alloys and aluminum metal matrix composites [J]. Transactions of Nonferrous Metals Society of China, 2021, 31: 3281−3309.

[14] LIU Fen-jun, LI Ya-peng, SUN Zhi-yong, JI Yan. Corrosion resistance and tribological behavior of particles reinforced AZ31 magnesium matrix composites developed by friction stir processing [J]. Journal of Materials Research and Technology, 2021, 11: 1019−1030.

[15] SATHISKUMAR R, DINAHARAN I, MURUGAN N, VIJAY S J. Influence of tool rotational speed on microstructure and sliding wear behavior of Cu/B_4C surface composite synthesized by friction stir processing [J]. Transactions of Nonferrous Metals Society of China, 2015, 25: 95−102.

[16] ESTHER I, DINAHARAN I, MURUGAN N. Microstructure and wear characterization of AA2124/4wt.%B_4C nano-composite coating on Ti−6Al−4V alloy using friction surfacing [J]. Transactions of Nonferrous Metals Society of China, 2019, 29: 1263−1274.

[17] XIONG Yong-jun, QIU Zi-li, LI Rui-di, YUAN Tie-chui, WU Hong, LIU Jin-hui. Preparation of ultra-fine grain Ni−Al−WC coating with interlocking bonding on austenitic stainless steel by laser clad and friction stir processing [J]. Transactions of Nonferrous Metals Society of China, 2015, 25: 3685−3693.

[18] PADHY G K, WU C S, GAO S. Friction stir based welding and processing technologies-processes, parameters, microstructures and applications: A review [J]. Journal of Materials Science & Technology, 2018, 34: 1−38.

[19] LI Jun-chen, LI Yu-long, WANG Fei-fan, MENG Xiang-chen, WAN Long, DONG Zhi-bo, HUANG Yong-xian. Friction stir processing of high-entropy alloy reinforced aluminum matrix composites for mechanical properties enhancement [J]. Materials Science & Engineering A, 2020, 792: 139755.

[20] GAO Ji-cheng, WANG Xuan, ZHANG Sun-yi, YU Liang, ZHANG Jian-feng, SHEN Yi-fu. Producing of FeCoNiCrAl high-entropy alloy reinforced Al composites via friction stir processing technology [J]. International Journal of Advanced Manufacturing Technology, 2020, 110: 569−580.

[21] YANG Xiao, YAN Zhi-feng, DONG Peng, CHENG Bu-yun, ZHANG Jie, ZHANG Ting-ting, ZHANG Hong-xia, WANG Wen-xian. Surface modification of aluminum alloy by incorporation of AlCoCrFeNi high entropy alloy particles via underwater friction stir processing [J]. Surface & Coatings Technology, 2020, 385: 125438.

[22] YANG Xiao, DONG Peng, YAN Zhi-feng, CHENG Bu-yun, ZHAI Xin, CHEN Hong-sheng, ZHANG Hong-xia, WANG Wen-xian. AlCoCrFeNi high-entropy alloy particle reinforced 5083Al matrix composites with fine grain structure fabricated by submerged friction stir processing [J]. Journal of Alloys and Compounds, 2020, 836: 155411.

[23] YANG Xiao, ZHAI Xin, DONG Peng, YAN Zhi-feng, CHENG Bu-yun, ZHANG Hong-xia, WANG Wen-xian. Interface characteristics of high-entropy alloy/Al−Mg composites by underwater friction stir processing [J]. Materials Letters, 2020, 275: 128200.

[24] YEH Jien-wei. Alloy design strategies and future trends in high-entropy alloys [J]. JOM, 2013, 65: 1759−1771.

[25] KATAKAM S, JOSHI S S, MRIDHA S, MUKHERJEE S, DAHOTRE N B. Laser assisted high entropy alloy coating on aluminum: Microstructural evolution [J]. Journal of Applied Physics, 2014, 116: 104906.

[26] SHON Y K, JOSHI S S, KATAKAM S, SHANKER RAJAMURE R, DAHOTRE N B. Laser additive synthesis of high entropy alloy coating on aluminum: Corrosion behavior [J]. Materials Letters, 2015, 142: 122−125.

[27] LIU Yun-zi, CHEN Jian, LI Zhao, WANG Xian-hui, FAN Xin-hui, LIU Jiang-nan. Formation of transition layer and its effect on mechanical properties of AlCoCrFeNi high-entropy alloy/Al composites [J]. Journal of Alloys and Compounds, 2019, 780: 558−564.

[28] NIU Yan-xia, LE Qi-chi, NING Fang-kun, HOU Jian, JIA Yong-hui. Strain induced dynamic recrystallization nucleation of ZA21 magnesium alloy during compression process at low and medium temperatures [J]. Journal of Materials Research and Technology, 2020, 9: 340−346.

[29] HUANG Li-ying, WANG Kuai-she, WANG Wen, YUAN Jie, QIAO Ke, YANG Tao, PENG Pai, LI Tian-qi. Effects of grain size and texture on stress corrosion cracking of friction stir processed AZ80 magnesium alloy [J]. Engineering Failure Analysis, 2018, 92: 392−404.

[30] LI Yu-lu, ZHAO Yue, SHEN Lin, WU Hao, ZHU He-gou. Microstructure and mechanical properties of in situ (TiC + SiC)/FeCrCoNi high entropy alloy matrix composites [J]. Journal of Iron and Steel Research International, 2021, 28: 496−504.

[31] WANG Wen, HAN Peng, PENG Pai, ZHANG Ting, LIU Qiang, YUAN Sheng-nan, HUANG Li-ying, YU Hai-liang,

QIAO Ke, WANG Kuai-she. Friction stir processing of magnesium alloys: A review [J]. Acta Metallurgica Sinica (English Letters), 2020, 33: 43−57.

[32] KHANDELWAL A, MANI K, SRIVASTAVA N, GUPTA R, CHAUDHARI G P. Mechanical behavior of AZ31/Al_2O_3 magnesium alloy nanocomposites prepared using ultrasound assisted stir casting [J]. Composites: Part B, 2017, 123: 64−73.

[33] KHODABAKHSHI F, ARAB S M, ŠVEC P, GERLICH A P. Fabrication of a new Al−Mg/graphene nanocomposite by multi-pass friction stir processing: Dispersion, microstructure, stability, and strengthening [J]. Materials Characterization, 2017, 132: 92−107.

[34] SANATY-ZADEH A. Comparison between current models for the strength of particulate-reinforced metal matrix nanocomposites with emphasis on consideration of Hall−Petch effect [J]. Materials Science and Engineering A, 2012, 531: 112−118.

[35] JAMSHIDIJAM M, AKBARI-FAKHRABADI A, MASOUDPANAH S M, HASANI G H, MANGALARAJA R V. Wear behavior of multiwalled carbon nanotube/AZ31 composite obtained by friction stir processing [J]. Tribology Transactions, 2013, 56: 827−832.

[36] MAZAHERI Y, KARIMZADEH F, ENAYATI M H. A novel technique for development of A356/Al_2O_3 surface nanocomposite by friction stir processing [J]. Journal of Materials Processing Technology, 2011, 211: 1614−1619.

[37] SUN H Q, SHI Y N, ZHANG M X. Wear behaviour of AZ91D magnesium alloy with a nanocrystalline surface layer [J]. Surface & Coatings Technology, 2008, 202: 2859−2864.

[38] MAZAHERI Y, JALILVAND M M, HEIDARPOUR A, JAHANI A R. Tribological behavior of AZ31/ZrO_2 surface nanocomposites developed by friction stir processing [J]. Tribology International, 2020, 143: 106062.

[39] CAO Xiong, SHI Qing-yu, LIU Da-meng, FENG Zhi-li, LIU Qu, CHEN Gao-qiang. Fabrication of in situ carbon fiber/aluminum composites via friction stir processing: Evaluation of microstructural, mechanical and tribological behaviors [J]. Composites: Part B, 2018, 139: 97−105.

搅拌摩擦加工制备 AZ31/CoCrFeNi 复合材料的组织、力学性能和磨损性能

王 文，方 园，彭 湃，张志娟，韩 鹏，张 婷，刘志浩，关肖虎，王 智，乔 柯，王快社

西安建筑科技大学 功能材料加工国家与地方联合工程研究中心，西安 710055

摘 要：采用搅拌摩擦加工工艺制备 CoCrFeNi 高熵合金颗粒增强 AZ31 镁基复合材料。采用 OM、SEM、EDS 和 EBSD 对复合材料的微观结构进行表征。通过拉伸、显微硬度和干滑动磨损实验研究复合材料的力学性能和磨损性能。结果表明，高熵合金颗粒分布均匀，与镁基体具有良好的冶金结合。复合材料的屈服强度、抗拉强度和硬度分别比母材高 80 MPa、46 MPa 和 HV 54.9。细晶强化是主要的强化机制，对屈服强度的贡献率为 43.9%。复合材料的平均摩擦因数由母材的 0.331 降低到 0.240，磨损机制由母材的黏着磨损转变为磨粒磨损。

关键词：搅拌摩擦加工；高熵合金颗粒；镁基复合材料；界面层；拉伸性能；磨损性能

(Edited by Xiang-qun LI)